Comparison of the numerical scheme with previous rotating SWE numerics of Dillingham, Armenio & La Rocca, Huang & Hsiung

by H. Alemi Ardakani & T. J. Bridges

Department of Mathematics, University of Surrey, Guildford GU2 7XH UK

— October 22, 2010—

Abstract

The fully-implicit space-centred numerical scheme developed by Alemi Ardakani & Bridges [6] is compared with the numerical results in the literature of Dillingham [9], Armenio & La Rocca [7] and Huang-Hsiung [11].

1 Introduction

Sloshing in shallow water relative to a rotating frame has been simulated numerically using a number of different methods. Dillingham [9] uses Glimm's method. Glimm's method is very effective in treating a large number of travelling hydraulic jumps, but the solutions are discontinuous. Armenio points out in the discussion of the paper by Huang & Hsiung [10] that Glimm's method also suffers from a strong mass variation over time in a simulation. Armenio & La Rocca [7] have used space-time conservation elements which have excellent conservation properties. They find that the method works very well for the simulation of both standing waves and hydraulic jumps, and the speed of travelling hydraulic jumps is well predicted even for large amplitudes of excitation. Huang & Hsiung [10, 11, 12] have used flux-vector splitting. This method involves computing eigenvalues of the Jacobian matrices, and is effective for tracking multi-directional characteristics. Their numerical results are qualitatively in agreement with Dillingham [9].

Our strategy for computing shallow-water sloshing is threefold. We want a method which extends easily to the case of two-horizontal space dimensions. Secondly, we want a method that is both implicit and has some numerical dissipation. Thirdly, we want a method which generalizes easily to the case of coupled vessel-fluid motion. For one horizontal space dimension there are a number of methods that could be used. We first implemented the Preissmann scheme and found it to have excellent properties. The Preissmann scheme is also very effective for transcritical flows. However, there are problems with extending the Preissmann scheme to two horizontal space dimensions.

Instead we use a fully-implicit spatially-centred finite difference scheme which leads to a block tridiagonal coefficient matrix. It is similar to a one-dimensional version of the Abbott-Ionescu scheme and the Leendertse scheme which are both widely used in open channel hydraulics.

The scheme has numerical dissipation, but the form of the dissipation is similar to the action of viscosity. The truncation error is of the form of the heat equation and so is strongly wavenumber dependent. Moreover the numerical dissipation follows closely the hydraulic structure of the equations. See the technical report Alemi Ardakani & Bridges [5] for an analysis of the form of the numerical dissipation. The numerical dissipation is helpful for eliminating transients and spurious high-wavenumber oscillation in the formation of travelling hydraulic jumps.

In this technical report we compare the numerical results generated by this scheme with the previous results in the literature.

2 Comparison with Dillingham's SWEs

Our first numerical experiment is to compare the computations using the surface SWEs with Dillingham's SWEs. In order to facilitate comparison the same numerical method is used for both, with the only difference being the choice of $a(x,t), b(x,t)$ for the surface SWEs and the choice $a(x,t)^D, b(x,t)^D$ for the case of Dillingham's SWEs. Fix data as shown in the first row of Table 1. Then with quiescent initial conditions a comparison between the two systems is shown in Figures 1 and 2. A particular value of x is chosen ($x = 0.4\,m$) and the time dependence of $h(x,t)$ at that location is plotted as a function of time.

The results diverge after some time. The error is predominantly amplitude error, but then at larger times, some phase errors appear. $|d_2| = 0.5\,m$ in Figure 1, and $|d_2|$ is 10 times smaller in Figure 2. The larger divergence between the two results when $|d_2|$ is small confirms the prediction based on the analysis of the equations in [6].

3 Comparison with the ALR SWEs

Armenio & La Rocca [7] present numerical simulations using the ALR SWEs

$$\overline{u}_t + \overline{u}\,\overline{u}_x + a(x,t)^{ALR} h_x = b(x,t;y)^{ALR}\,, \tag{3.1}$$

with

$$\begin{aligned} a(x,t)^{ALR} &= g\cos\theta + \dot{\Omega}(x+d_1) - \Omega^2(h+d_2) + 2\Omega\overline{u}\,, \\ b(x,t;y)^{ALR} &= -g\sin\theta - 2\Omega h\overline{u}_x + \dot{\Omega}(y-h+d_2) + \Omega^2(x+d_1)\,. \end{aligned} \tag{3.2}$$

With appropriate change of notation, this is equation (18) in [7].

They compare their results with both in house experiments and direct numerical simulations of the two-dimensional flowfield using a marker-and-cell type method including Reynold's averaging (called RANSE in their paper). Here we will compare numerical simulations of the surface SWEs with the ALR SWEs simulations, and by inference also compare with their experiments and RANSE simulations.

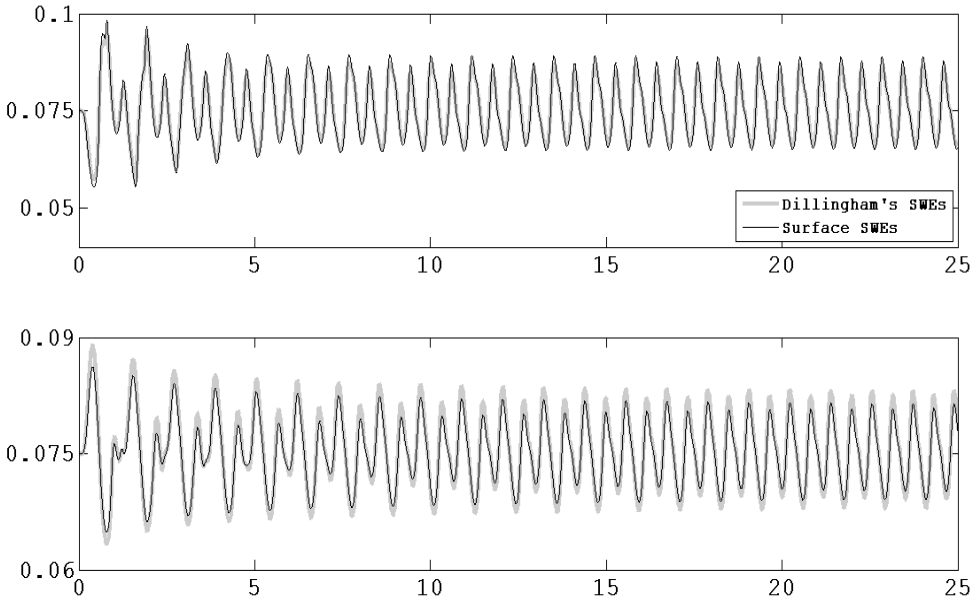

Figure 1: Surface elevation at $x = 0.40\,m$ with parameters listed in Table 1 showing a comparison between the surface SWEs and Dillingham's SWEs. $d_2 = 0.50\,m$ and $d_2 = -0.50\,m$ for upper and lower figures respectively. The horizontal axis is time in *sec* and the vertical axis is wave height in m.

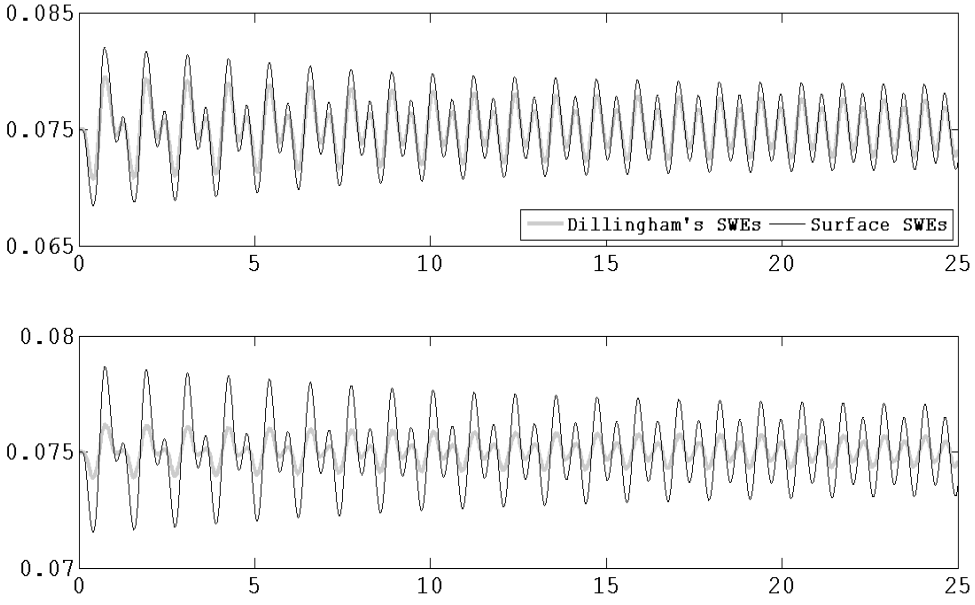

Figure 2: Same as Figure 1 with $d_2 = 0.05\,m$ and $d_2 = -0.05\,m$ for the upper and lower figures respectively.

Table 1: Input data for the numerical experiments in Figures 1–10. In all cases, $q_1(t) = q_2(t) = 0$ and the initial conditions are $h(x,0) = h_0$ and $U(x,0) = 0$. The first natural frequency ω_1 is listed to two significant figures using $\omega_m = \sqrt{gh_0}\, m\pi/L$ with $g = 9.81\, m/s^2$.

Figure	L	h_0	d_1	d_2	δ	ω	ω_1	Δx	Δt
	(m)	(m)	(m)	(m)	(rad)	(rad/sec)	(rad/sec)	(m)	(sec)
1	0.5	0.075	-0.25	± 0.5	$\pi/180$	10.77	5.39	0.005	0.005
2	0.5	0.075	-0.25	± 0.05	$\pi/180$	10.77	5.39	0.005	0.005
3	0.5	0.025	-0.25	0.048	varying	varying	3.11	0.005	0.005
4	0.5	0.025	-0.25	0.048	$0.91\pi/180$	3.98	3.11	0.005	0.005
7	0.5	0.05	-0.25	0.048	$0.91\pi/180$	5.05	4.40	0.005	0.005
8	0.5	0.05	-0.25	0.048	$0.91\pi/180$	5.56	4.40	0.005	0.005
9	0.5	0.025	-0.25	0.048	$1.70\pi/180$	3.98	3.11	0.005	0.005
10	1	0.06	-0.5	-0.522	0.067	2.40	2.41	0.005	0.005

[7] point out that the experiments were not able to produce strictly harmonic forcing, and so they used the experimental tank motion as input into the numerics rather than a strict harmonic function. Here we will use a strictly harmonic forcing for the angular motion, and this should be taken into account in the comparison.

The two graphs in Figure 3 show the computational results corresponding to Figures 13 and 14 in [7]. The parameter values are listed in the third row of Table 1. The only difference between the upper and lower data sets is the forcing amplitude. It is 0.91^o in lower graph in Figure 3 and 1.7^o in the upper graph. The figure shows the maximum wave height ($|h_{max} - h_{min}|/L$) as a function of the forcing frequency. The natural frequency is approximately π, and that is typically where the maximum amplitude occurs. The comparison is qualitatively good but the slope is much more gentle in these figures. This difference could be due to either the change in forcing, or the effect of transients.

The time dependence of the wave height at a fixed value of x ($x = 0.4\, m$) is plotted in Figure 4. The parameters are the same as in Figure 3 (at the lower forcing amplitude) but with the forcing frequency fixed at $\omega = 3.98\, rad/sec$. Note that there are transient values of the wave height which exceed the steady state (periodic) maximum amplitude. The appearance of large transients and eventual settling down to steady state motion is precisely what occurs in Figure 15 of [7]. This behaviour is consistent with the RANSE simulations although both the RANSE simulations and the experiments show the appearance of additional harmonics. To see what is happening in the transient versus steady state regimes in Figure 4, snapshots of the vessel showing the spatial dependence of the waveheight are shown at a sequence of times in Figures 5 and 6. The initial transient region corresponds to a travelling hydraulic jump, and it settles down to a periodic standing wave.

Figures 7 and 8 show the dramatic difference between forcing near the natural frequency and forcing away from the natural frequency. Figure 7 has parameter values

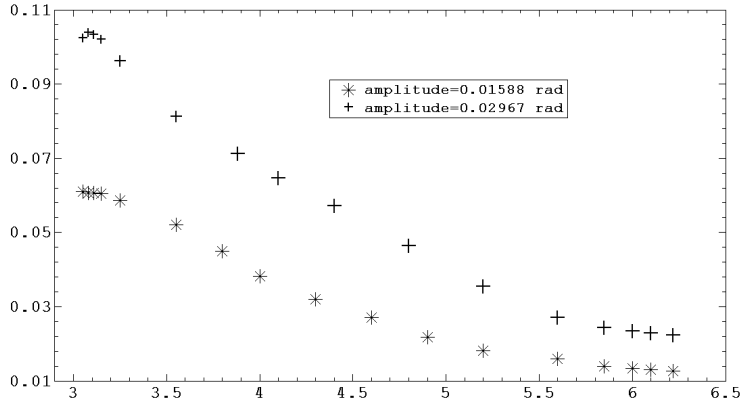

Figure 3: Comparison of the computation with the surface SWEs with Figure 13 and Figure 14 of [7]. The horizontal axis is time in frequency rad/sec and the vertical axis is nondimensional wave height at $x = 0.4m$ in m.

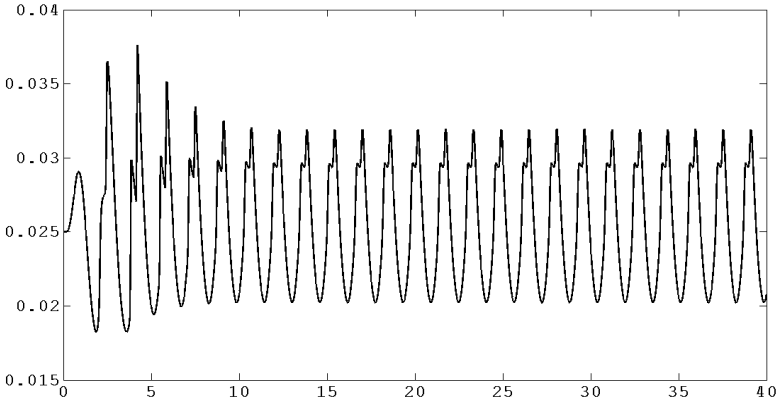

Figure 4: Comparison of the computation with the surface SWEs with Figure 15 of [7]. Data tabulated in Table 1. The horizontal axis is time in sec and the vertical axis is wave height in m at $x = 0.4m$.

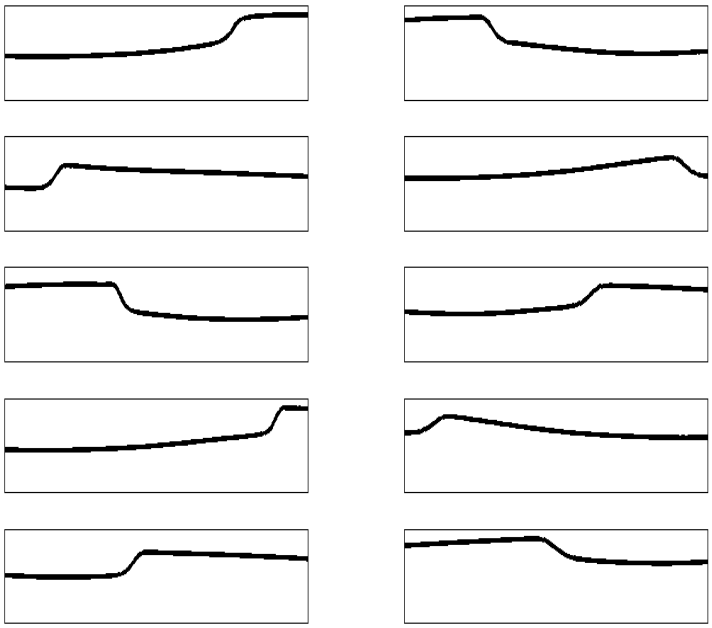

Figure 5: Wave profiles computed using the surface SWEs showing the free surface as a function of x at $t = 2.5\,s$, $t = 3.0\,s$, $t = 3.5\,s$, $t = 4.1\,s$, $t = 4.5\,s$ for the left column from top to bottom and at $t = 5.1\,s$, $t = 5.6\,s$, $t = 6.0\,s$, $t = 6.4\,s$, $t = 6.9\,s$ for the right column from top to bottom. Parameter values the same as in Figure 4.

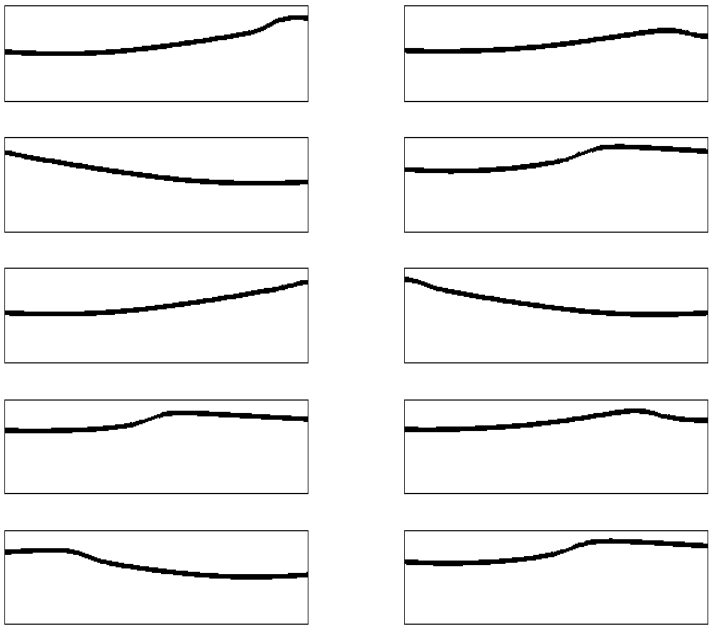

Figure 6: Continuation of Figure 5. Wave profiles computed using the surface SWEs showing the free surface as a function of x. The snapshots are at $t = 9.0\,s$, $t = 9.7\,s$, $t = 10.5\,s$, $t = 10.9\,s$, $t = 11.5\,s$ for the left column from top to bottom and at $t = 12.0\,s$, $t = 12.4\,s$, $t = 12.9\,s$, $t = 13.5\,s$, $t = 14.0\,s$ for the right column from top to bottom.

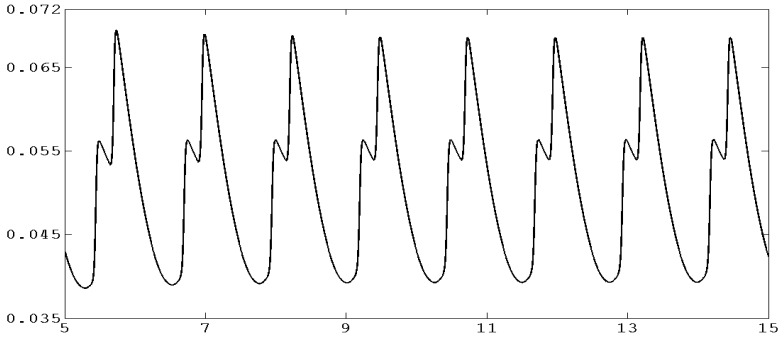

Figure 7: Comparison of the computation with the surface SWEs with Figure 20 of [7]. Data are $h_0 = L/10$, $\omega = 5.05\,rad/sec$ and $\delta = 0.91^o$. The forcing frequency is very close to the natural frequency. The horizontal axis is time in sec and the vertical axis is wave height in m at $x = 0.4m$.

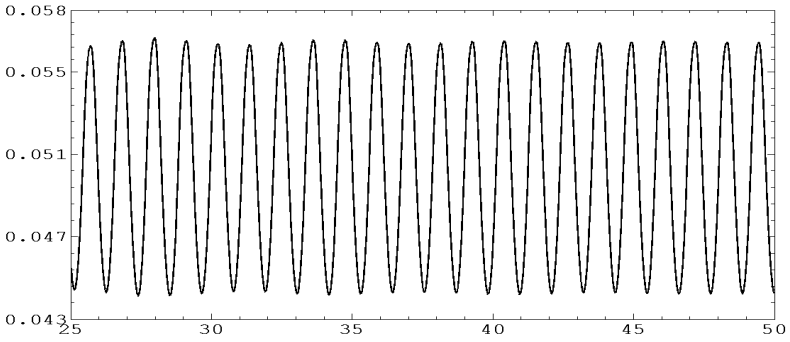

Figure 8: Comparison of the computation with the surface SWEs with Figure 21 of [7]. The data are $h_0 = L/10$, $\omega = 5.56\, rad/sec$ (away from natural frequency), $\delta = 0.91^o$. The horizontal axis is time in sec and the vertical axis is wave height in m at $x = 0.4m$.

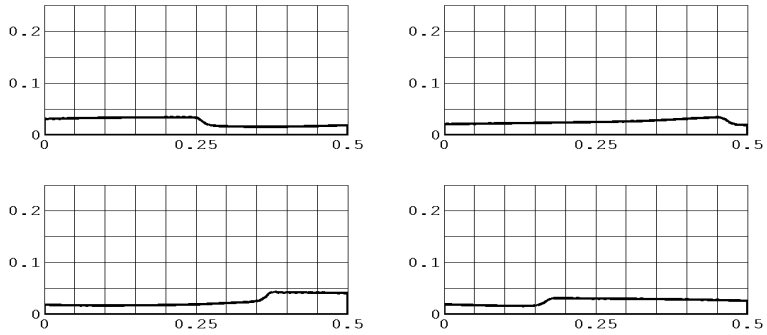

Figure 9: Comparison of the computation with the surface SWEs with Figure 17 of [7]. Data tabulated in Table 1.

corresponding to Figure 20 in [7]: $h_0/L = 0.10$, $\omega = 5.05\, rad/sec$ (close to resonance) and $\delta = 0.91^o$. The time history of the wave height is shown at $x = 0.40\, m$. The qualitative agreement with Figure 20 in [7] is excellent. However, their RANSE simulations show the presence of several additional wave modes. This comparison is an example where the SWEs capture the principal qualitative properties of the waves but not the detail.

Figure 8 shows a computation with the surface SWEs with parameter values associated with Figure 21 in [7]. Same data as in Figure 7 but with $\omega = 5.56$ rad/sec, so it is away from resonance. In this case the motion is much more regular. Again this simulation compares very well with the SWE simulation in Figure 21 of [7]. In this case the RANSE simulations and the experiments had an additional high frequency component, which gave the appearance of beating.

Figure 9 shows spatial dependence of the wave profiles at parameter values corresponding to Figure 17 in [7]. The agreement between the current simulations and [7] in this case is excellent.

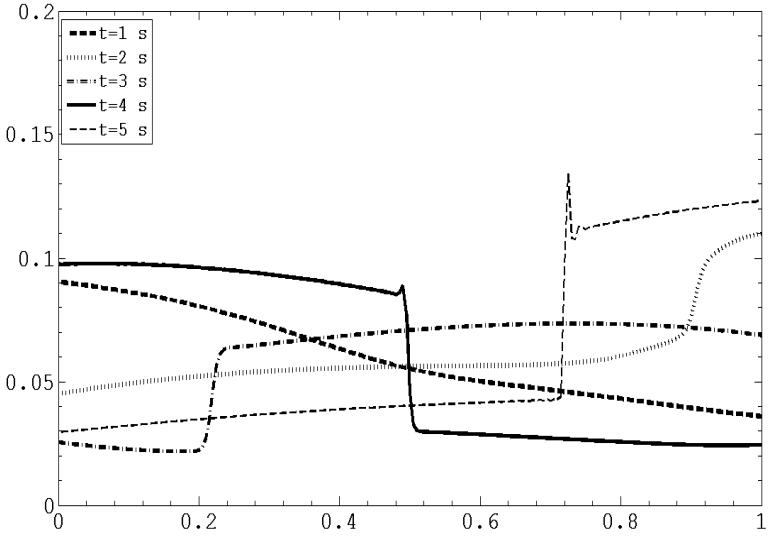

Figure 10: Comparison of the numerics based on the surface SWEs with Figure 6 of [11]. The horizontal axis is x in m and the vertical axis is water depth in m.

4 Comparison with Huang & Hsiung [11]

The SWEs used in [11] are almost the same as Dillingham's. For pure rotation, they have an example with a strong hydraulic jump which provides a good test of a numerical scheme. Figure 10 shows a simulation using the surface SWEs with parameter values as in Figure 6 of [11]. The frequency is very close to the first natural frequency ($\omega_1 \approx 2.41\, rad/sec$) and, as is typically the case for forcing near the natural frequency, a travelling hydraulic jump forms. The numerics captures the travelling hydraulic jump very well. Surprisingly the results also are close to those of [11], particularly the phase, although the amplitudes differ especially for later times.

5 Concluding remarks

Numerical results, including the effect of the centre of rotation, combined rotation-translation forcing, and sloshing on the London eye, obtained by the new numerical scheme are reported in [6].

References

[1] `http://personal.maths.surrey.ac.uk/st/T.Bridges/SLOSH/`

[2] H. Alemi Ardakani. *Rigid-body motion with interior shallow-water sloshing*, PhD Thesis, University of Surrey (2010).

[3] H. Alemi Ardakani & T.J. Bridges. *Review of the Huang-Hsiung rotating two-dimensional shallow-water equations*, Tech. Rep., Department of Mathematics, University of Surrey (2009).

[4] H. Alemi Ardakani & T.J. Bridges. *Review of the Armenio-LaRocca two-dimensional shallow-water equations*, Tech. Rep., Department of Mathematics, University of Surrey (2009).

[5] H. Alemi Ardakani & T.J. Bridges. *Shallow water sloshing in rotating vessels: details of the numerical algorithm*, Tech. Rep., Department of Mathematics, University of Surrey (2009).

[6] H. Alemi Ardakani & T.J. Bridges. *Shallow-water sloshing in rotating vessels undergoing prescribed rigid-body motion in two dimensions*, Preprint (2010).

[7] V. Armenio & M. La Rocca. *On the analysis of sloshing of water in rectangular containers: numerical study and experimental validation*, Ocean Eng. **23** 705–739 (1996).

[8] S.-C. Chang. *The method of space-time conservation elements and solution element – a new approach for solving the Navier-Stokes and Euler equations*, J. Comp. Phys. **119** 295–324 (1995).

[9] J. Dillingham. *Motion studies of a vessel with water on deck*, Marine Technology **18** 38–50 (1981).

[10] Z.J. Huang & C.C. Hsiung. *Application of the flux difference splitting method to compute nonlinear shallow water flow on deck*, In the Proc. 9th Int. Workshop on Water Waves and Floating Bodies, Japan, 17-20 April 1994, pp. 83–87, IWWWFB (1994).

[11] Z.J. Huang & C.C. Hsiung. *Nonlinear shallow water flow on deck*, J. Ship Research **40** 303–315 (1996).

[12] Z.J. Huang & C.C. Hsiung. *Nonlinear shallow-water flow on deck coupled with ship motion*. In the Twenty-First Symposium on Naval Hydrodynamics, pp. 220–234, National Academies Press (1997).